remote sensing

MDPI

Article

Concept and Design of Martian Far-IR ORE Spectrometer (MIRORES)

Jakub Ciazela [1], Jaroslaw Bakala [2], Miroslaw Kowalinski [2,*], Stefan Plocieniak [2], Natalia Zalewska [2], Bartosz Pieterek [3], Tomasz Mrozek [2], Marta Ciazela [1], Grzegorz Paslawski [1], Marek Steslicki [2], Zaneta Szaforz [2], Jaromir Barylak [2], Mateusz Kuzaj [4], Alessandro Maturilli [5], Joern Helbert [5], Andrzej Muszynski [3], Miroslaw Rataj [2], Szymon Gburek [2], Mateusz Jozefowicz [6] and Dariusz Marciniak [1]

[1] Research Centre in Wrocław, Institute of Geological Sciences, Polish Academy of Sciences, Podwale 75, 50-449 Wrocław, Poland; j.ciazela@twarda.pan.pl (J.C.); mc@cbk.pan.wroc.pl (M.C.); g.paslawski@twarda.pan.pl (G.P.); dariusz.marciniak@twarda.pan.pl (D.M.)
[2] Space Research Centre, Polish Academy of Sciences, ul. Bartycka 18A, 00-716 Warsaw, Poland; jb@cbk.pan.wroc.pl (J.B.); sp@cbk.pan.wroc.pl (S.P.); natalia@cbk.waw.pl (N.Z.); tmrozek@cbk.pan.wroc.pl (T.M.); sm@cbk.pan.wroc.pl (M.S.); zs@cbk.pan.wroc.pl (Z.S.); jbarylak@cbk.pan.wroc.pl (J.B.); rataj@cbk.waw.pl (M.R.); sg@cbk.pan.wroc.pl (S.G.)
[3] Institute of Geology, Adam Mickiewicz University, ul. Bogumiła Krygowskiego 12, 61-680 Poznań, Poland; barpie@amu.edu.pl (B.P.); anmu@amu.edu.pl (A.M.)
[4] Faculty of Fundamental Problems of Technology, Wroclaw University of Science and Technology, Wybrzeże Stanisława Wyspiańskiego 27, 50-370 Wrocław, Poland; 236777@student.pwr.edu.pl
[5] Institut für Planetenforschung, Deutsches Zentrum für Luft- und Raumfahrt (DLR), Rutherfordstrasse 2, D-12489 Berlin, Germany; alessandro.maturilli@dlr.de (A.M.); joern.helbert@dlr.de (J.H.)
[6] European Space Foundation, Grodzka 42/1, 31-044 Kraków, Poland; m.jozefowicz@spacefdn.com
* Correspondence: mk@cbk.pan.wroc.pl

Abstract: Sulfide ores are a major source of noble (Au, Ag, and Pt) and base (Cu, Pb, Zn, Sn, Co, Ni, etc.) metals and will, therefore, be vital for the self-sustainment of future Mars colonies. Martian meteorites are rich in sulfides, which is reflected in recent findings for surface Martian rocks analyzed by the Spirit and Curiosity rovers. However, the only high-resolution (18 m/pixel) infrared (IR) spectrometer orbiting Mars, the Compact Reconnaissance Imaging Spectrometer for Mars (CRISM), onboard the Mars Reconnaissance Orbiter (MRO), is not well-suited for detecting sulfides on the Martian surface. Spectral interference with silicates impedes sulfide detection in the 0.4–3.9 μm CRISM range. In contrast, at least three common hydrothermal sulfides on Earth and Mars (pyrite, chalcopyrite, marcasite) have prominent absorption peaks in a narrow far-IR (FIR) wavelength range of 23–28 μm. Identifying the global distribution and chemical composition of sulfide ore deposits would help in choosing useful targets for future Mars exploration missions. Therefore, we have designed a new instrument suitable for measuring sulfides in the FIR range called the Martian far-IR Ore Spectrometer (MIRORES). MIRORES will measure radiation in six narrow bands (~0.3 μm in width), including three bands centered on the sulfide absorption bands (23.2, 24.3 and 27.6 μm), two reference bands (21.5 and 26.1) and one band for clinopyroxene interference (29.0 μm). Focusing on sulfides only will make it possible to adapt the instrument size (32 × 32 × 42 cm) and mass (<10 kg) to common microsatellite requirements. The biggest challenges related to this design are: (1) the small field of view conditioned by the high resolution required for such a study (<20 m/pixel), which, in limited space, can only be achieved by the use of the Cassegrain optical system; and (2) a relatively stable measurement temperature to maintain radiometric accuracy and enable precise calibration.

Keywords: sulfides; ore minerals; Mars; microsatellite; far-infrared spectroscopy

Citation: Ciazela, J.; Bakala, J.; Kowalinski, M.; Plocieniak, S.; Zalewska, N.; Pieterek, B.; Mrozek, T.; Ciazela, M.; Paslawski, G.; Steslicki, M.; et al. Concept and Design of Martian Far-IR ORE Spectrometer (MIRORES). *Remote Sens.* **2022**, *14*, 2799. https://doi.org/10.3390/rs14122799

Academic Editor: Louis Scuderi

Received: 28 April 2022
Accepted: 29 May 2022
Published: 10 June 2022

1. Introduction

In 2001, the European Space Agency (ESA) created the Aurora program aiming at a human mission to Mars in 2033 [1]. Despite a seven-year delay in the implementation of this program, ESA has successfully launched the first of two preparatory flagship missions (Exobiology on Mars (ExoMars)) and started activities related to the second mission (Mars Sample Return (MSR)). The MSR mission should be directly followed by the human mission and is intended to be a concerted effort of all humanity, organized together with NASA, the Japan Aerospace Exploration Agency (JAXA), the Indian Space Research Organization (ISRO), and the Russian Roscosmos [2,3].

Among the four strategic resources envisaged during the human stage of Solar System exploration, after water and propellants, ESA has listed base metals (e.g., Fe, Ti, Cu) and noble metals (e.g., platinum group elements, Au, Ag) [4]. Some chalcophile and siderophile metals are expected to be vital for the future colonization of Mars, and those used as conductors in electronic devices such as Cu, Ag, and Au, will be especially important. The key metals will have to be extracted in situ as flights between Earth and Mars are feasible only in a narrow time window of 50–150 days before Mars and Earth are in opposition, which only occurs every two years. Chalcophile and siderophile metals are hosted mostly in sulfides and oxides, and occasionally in platinum-group metal (PGM) minerals and native metals, which are all major sources of most noble metals (Au, Ag, Pt, and Pd) and base metals (Fe, Ti, V, Cr, Cu, Pb, Zn, Sn, Co, Ni, etc.) on Earth [5]. Among these, sulfides are the most important group of ore minerals [6] and are especially crucial for Cu, Ag, and Au.

Despite the lack of direct evidence, sulfide ore deposits are predicted to be present on Mars [7–10]. Rover data along with geochemical modeling suggest the presence of pyrite (FeS_2: cubic crystal system), marcasite (FeS_2: orthorhombic crystal system), and pyrrhotite ($Fe_{1-x}S$) at the Martian surface [11–13]. Furthermore, studies of Martian meteorites [14,15] show that the Martian crust is significantly enriched in chalcophile (sulfide-loving) elements compared to the Martian mantle. Martian meteorites host a variety of magmatic and hydrothermal sulfides [16–18], matching those from the sulfide ores on Earth.

To date, however, it has been difficult to localize ore-forming minerals on Mars based on the available remote-sensing instruments such as the Compact Reconnaissance Imaging Spectrometer for Mars (CRISM; operating in a wavelength range of 0.4–3.9 μm), launched in 2005 on the Mars Reconnaissance Orbiter (MRO); the Observatoire pour la Minéralogie, l'Eau, les Glaces et l'Activité (OMEGA; 0.4–5.1 μm) and the Planetary Fourier Spectrometer (PFS; 1.3–45 μm), launched on Mars Express (MEX) in 200; or the Thermal Emission Spectrometer (TES; 0.3–2.9 and 6–50 μm), launched on Mars Global Surveyor in 1996. The mineral spectra of CRISM/MRO allow for a thorough mineral interpretation of investigated areas with a resolution of ~18 m/pixel, being one order of magnitude higher than the resolution of ~300 m/pixel provided previously by OMEGA/MEX [19]. However, although major sulfides have been found by rovers on the Mars surface, and their spectra are available through the USA Geological Survey (USGS) spectral library (https://speclab.cr.usgs.gov/spectral-lib.html, accessed on 27 April 2022), the weak spectral features of sulfides in the near-infrared (NIR) and interference with silicates impede sulfide detection in the NIR range available from CRISM. For example, pyrite exhibits only a broad shoulder just beyond 1 μm which, in addition, interferes with a similar shoulder displayed by clinopyroxene (Figure 1) [20]. This is crucial, as clinopyroxene is one of the several most abundant minerals on the Mars surface [21,22].

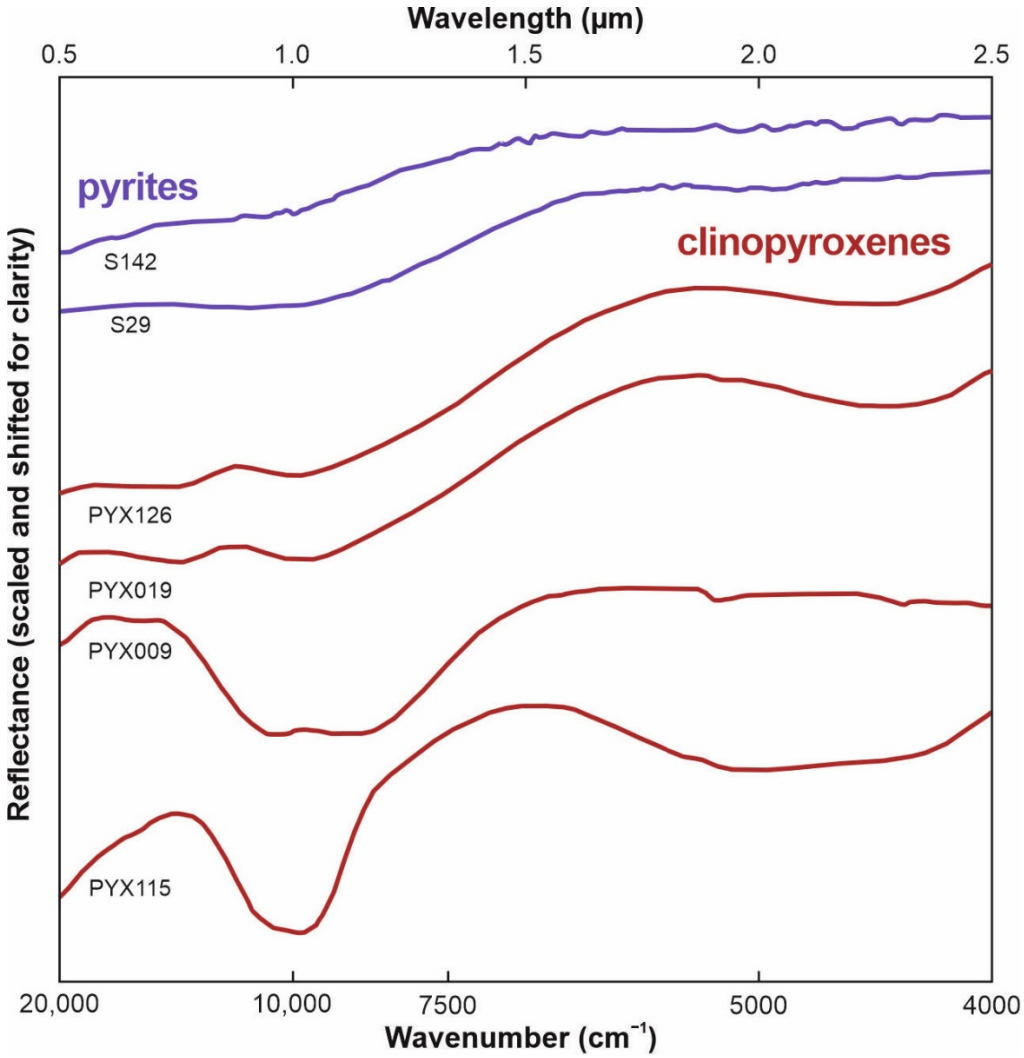

Figure 1. Near-infrared (NIR) spectra of pyrites S142 and S29 compared to those of clinopyroxenes PYX126, PYX019, PYX009 and PYX115, which are all described by Horgan et al. [20]. Note the lack of distinct spectral features in pyrites and their similarity to the NIR spectra of some clinopyroxenes. Considering the low pyrite abundances compared to those of clinopyroxene, pyrite is difficult to observe in the NIR range. The y axis has no numerical scale as the plots are shifted for clarity.

By contrast, the three most common hydrothermal sulfides on Earth and Mars (i.e., pyrite, chalcopyrite, and marcasite) possess prominent absorption bands in a narrow wavelength range of 23–28 μm [23–26]. The case is similar for pyrrhotite, troilite, and pentlandite [24], which are the most common magmatic sulfides in the Martian meteorites [27,28], even if they are less common in the context of large ore deposits. Importantly, the far-infrared (FIR) spectral features of the abovementioned sulfides have no significant interferences with rock-forming minerals in contrast to the currently available NIR range. The NIR spectral features of sulfides are lost in the spectral features of ubiquitous silicates including orthopyroxene, clinopyroxene, olivine, and plagioclase. Quartz may also occur locally on Mars [29] and trigonal quartz shows one of its minor peaks at 401 cm^{-1} (24.9 μm) [30], close to the pyrite peak, which is, however, beyond the measured pyrite band at 409–414 cm^{-1} (24.15–24.45 μm).

Although the PFS/MEX and TES/MGS cover the FIR spectral range, their spatial resolution of ~10 km and ~3 km, respectively, are not sufficient to search for ore deposits (Figure 2), which normally cover much smaller areas (up to hundreds of meters). Therefore, we designed a relatively inexpensive and simple Martian far-IR ORE Spectrometer

(MIRORES) based on pyroelectric detectors measuring six narrow (~0.3 μm) spectral bands obtained with diffraction grating, including three main bands centered at 23.2 μm (431 cm^{-1}), 24.3 μm (411.5 cm^{-1}), and 27.6 μm (362 cm^{-1}), two reference bands centered at 21.5 μm (465 cm^{-1}) and 26.1 μm (383 cm^{-1}), as well as one band for the interference with clinopyroxene at 29.0 μm (345 cm^{-1}). Measuring only six bands minimizes the required instrument dimensions to microsatellite size (32 × 32 × 42 cm) and mass (<10 kg). Although infrared spectroscopy methods have traditionally focused on the Earth atmospheric windows (3–5 μm and 8–14 μm), in recent years there has been increasing interest in longer wavelengths stimulated by space applications [31]. The largest challenge related to our design is, however, the small field of view conditioned by the high resolution we require (<20 m/pixel), which, in limited space, can only be achieved by the use of the Cassegrain optical system. Although it is being prepared for a Martian mission, our instrument may be adapted to measure sulfide ores on the Moon or large asteroids.

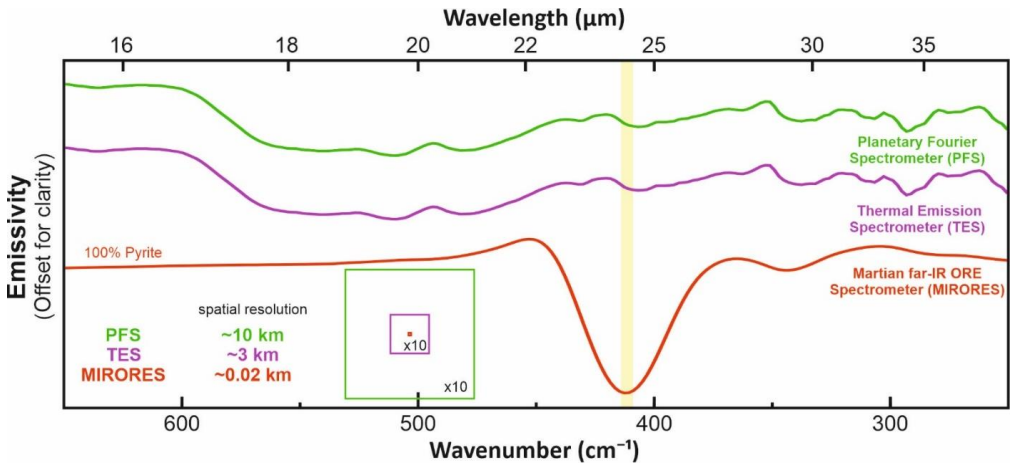

Figure 2. Simulation of observed emissivity spectra from 20 m × 20 m field covered by pyrite and surrounded by infinite area of basalts with shergottitic composition (see Section 3) as recorded by the Planetary Fourier Spectrometer (PFS), Thermal Emission Spectrometer (TES), and our MIRORES spectrometer. The simulations show that the orebodies similar in size to those on Earth would be impossible to detect with the far-IR spectrometers currently orbiting Mars due to the low spatial resolution of the spectrometers (see the bottom left corner of the figure).

2. Spectral Ranges and Interferences

The instrument will measure the FIR spectra of the Martian surface with the key detectors collecting signals from three narrow bands between 23 and 28 μm, where pyrite (24.3 μm = 412 cm^{-1}), marcasite (23.2 μm = 431 cm^{-1} on the slope), and chalcopyrite (27.6 μm = 362 cm^{-1}) show their main absorption lines. Three additional side detectors collect reference signals from narrow bands centered at 21.5, 26.1 and 29.0 μm (465, 383 and 345 cm^{-1}), where sulfides show no spectral features. However, the radiance received by the detectors depends on many factors, including solar geometry and slope inclination, which need to be normalized. This can be overcome by applying the band ratios of the signals received from the main detectors to the reference signals interpolated from the reference detectors. This will reduce the solar geometry and topographic effects on the remotely sensed data and is widely applied in ore prospecting with Landsat 8 and ASTER spectral bands on Earth [32]. Measurements in the FIR spectral range have two major advantages: (1) limited atmospheric interferences (Figures 3 and 4), and (2) strong absorption features of sulfides (Figure 5A) compared to common silicates (Figure 5B).

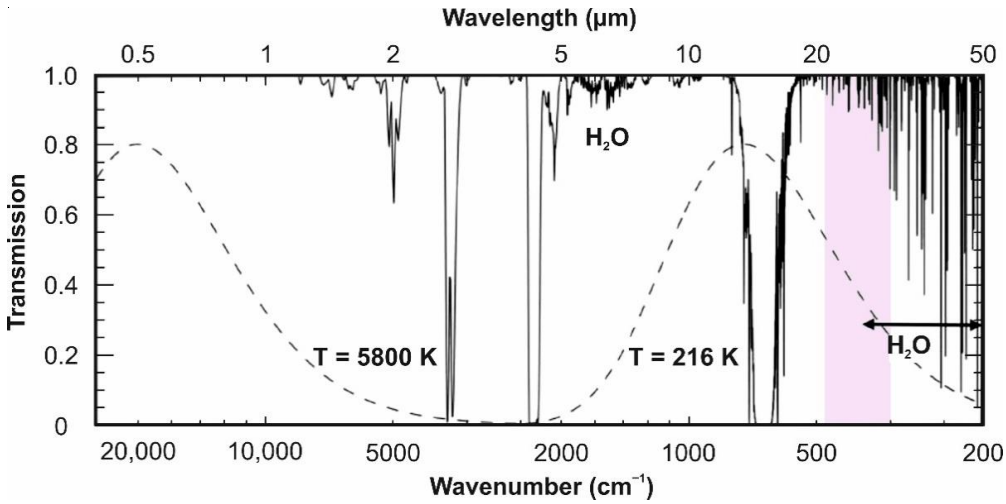

Figure 3. Synthetic infrared transmission spectrum for the atmosphere of Mars (clear of dust and aerosols), calculated assuming temperature structure and composition from the COSPAR Reference Atmosphere for Mars. The dashed lines show blackbody emission curves for temperatures of 5800 and 216 K, representative of the Sun and the Martian surface, respectively. Note the excellent atmospheric transmission in our target range of 21–30 μm (pink field). Modified from [33]. © IOP Publishing. Reproduced with permission. All rights reserved.

The Martian atmosphere is composed of CO_2 (96 vol.%), N_2 (1.9 vol.%), Ar (1.9 vol.%), and trace amounts of other gases including O_2, H_2O, and O_3 [33]. CO_2 shows a strong vibration–rotation absorption band centered around 15 μm (Figure 3), in which surface measurements on Mars are impossible, but pure CO_2 absorbs relatively little beyond that band. H_2O, which is a strong absorber on Earth typically containing ~40 kg·m^{-2} in the atmospheric column, is scarce on Mars with only 0.01–0.1 kg·m^{-2}. Although H_2O is not an issue in our target range of 23–28 μm, it may become a significant absorber at >30 μm (Figure 3) and selected lines <30 μm (Figure 4). On the whole, however, the transmittance of the Martian atmosphere in the FIR range is significantly higher than that of the Earth atmosphere (Figure 3). This is not the case only when larger amounts of dust are present in the Martian atmosphere during seasonal dust storms, which could then hinder our measurements. In normal conditions, dust opacity is only ~0.1 [34] and the absorption features of dust are weak in our target spectral range of 20–30 μm [35].

Considering the second advantage, the spectral features of sulfides in the FIR range are much stronger than the spectral features of any of the common Martian silicates known from the most abundant Martian meteorites, i.e., shergottites; that is, olivines, clinopyroxenes, orthopyroxenes, and plagioclase (Figures 4 and 5) [21]. This is a major advantage compared to the NIR range, where sulfides are nearly indistinguishable from pyroxenes (Figure 1). Sulfates, which are also ubiquitous on the surface of Mars, especially in water-rich environments [22,36,37], do not interfere with sulfides either (Figures 5C and 6B). Akaganeite, however, shows a peak centered at 414 cm^{-1} (24.2 μm) [38], which is close to pyrite (see Supplementary Figure S1A in Supplementary Material 1). Yet this is a rare mineral believed to form on Earth and Mars as an alteration of pyrrhotite [39]. The Curiosity rover detected akaganeite (as a minor component, <1.7 wt.%) only in samples where pyrrhotites (also minor, ~1 wt.%) were present, suggesting a genetic link between the two phases [13]. Therefore, the presence of akaganeite even increases our chances of finding sulfide mineralization. The case for some arsenides may be similar; for example, mimetite (418 cm^{-1} = 23.9 μm) [38], which occurs most of all in oxidation zones of metallic ores [40]. Hematite, which is also an ore mineral but is probably more common than sulfides on Mars [41], has its peak at 467 cm^{-1} (21.4 μm), far from the sulfide peaks (Supplementary Figure S1A). K-rich alkali feldspars, common in granites on Earth, such as microcline with a peak at 413 cm^{-1} (24.2 μm), would be more problematic for sulfide detection (see

Supplementary Figure S1C in Supplementary Material 1). These, however, even if not weathered to clay minerals, are associated with felsic silica-rich evolved magmas, which are rare in the recent history of Mars [41,42]. Among common secondary silicates, the only mineral interfering with sulfides may be prehnite (see Supplementary Figure S1B in Supplementary Material 1), which occurs on Mars [43–46]. Prehnite shows a weak absorption peak centered at 420 cm^{-1} (23.8 μm) near the pyrite peak and, therefore, larger amounts of prehnite could mimic a signal of smaller amounts of pyrite. For larger sulfide concentrations (>20%), to which MIRORES is dedicated, its potential interference with pyrite is nearly negligible. Similar could be the case for carbonates, which may constitute up to 2–5 wt.% of martian dust [47]. Magnesium-bearing carbonates, magnesite and dolomite, show very broad but relatively weak absorption features overlapping sulfides. In addition, these features are so broad that they extend to the reference detectors and therefore are easily distinguishable from sulfides (Figure 6C).

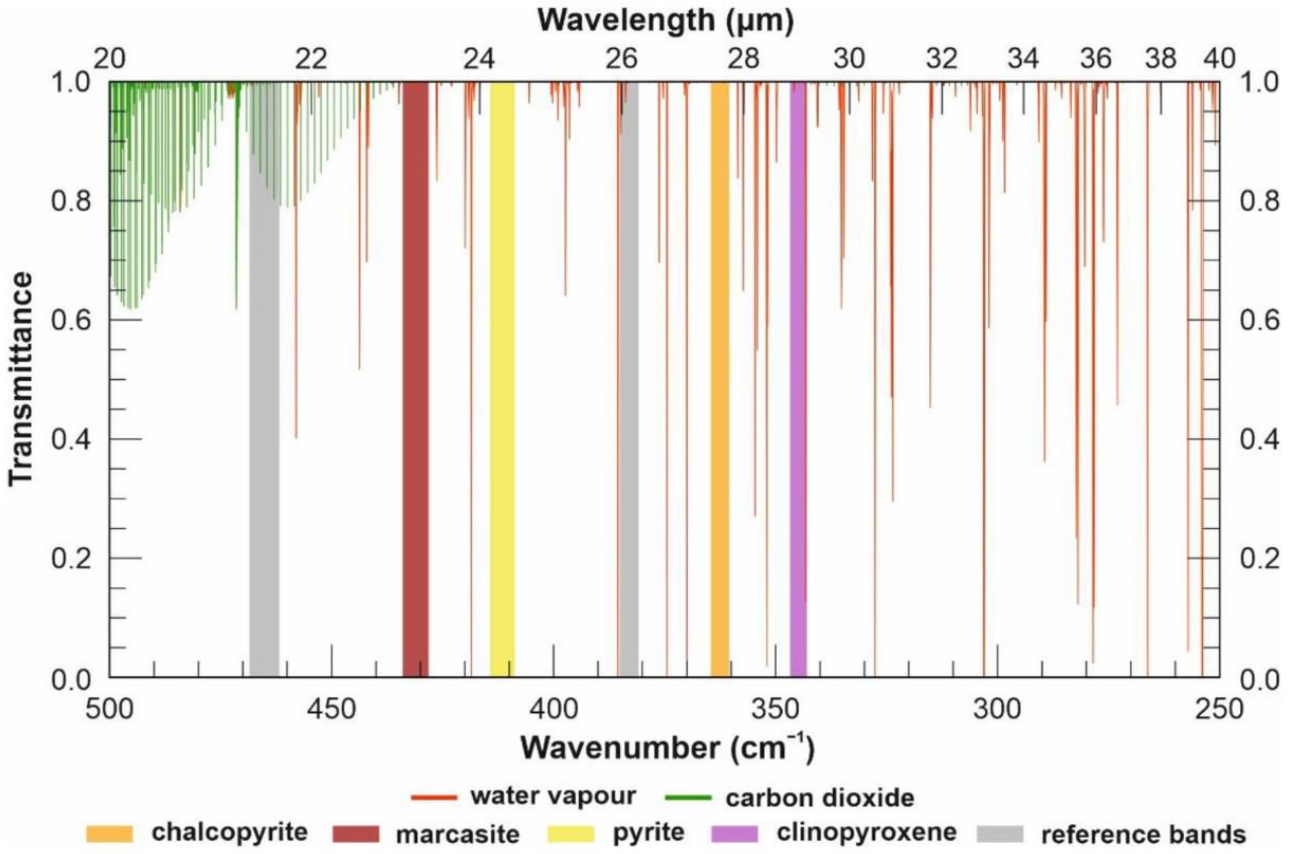

Figure 4. Exact positions of H_2O (red) and CO_2 (green) lines in the wavelength range covered by MIRORES. The values of H_2O and CO_2 absorption coefficients are from the HITRAN database [48], and details of the applied model are in Supplementary Material 2 (IDL script).

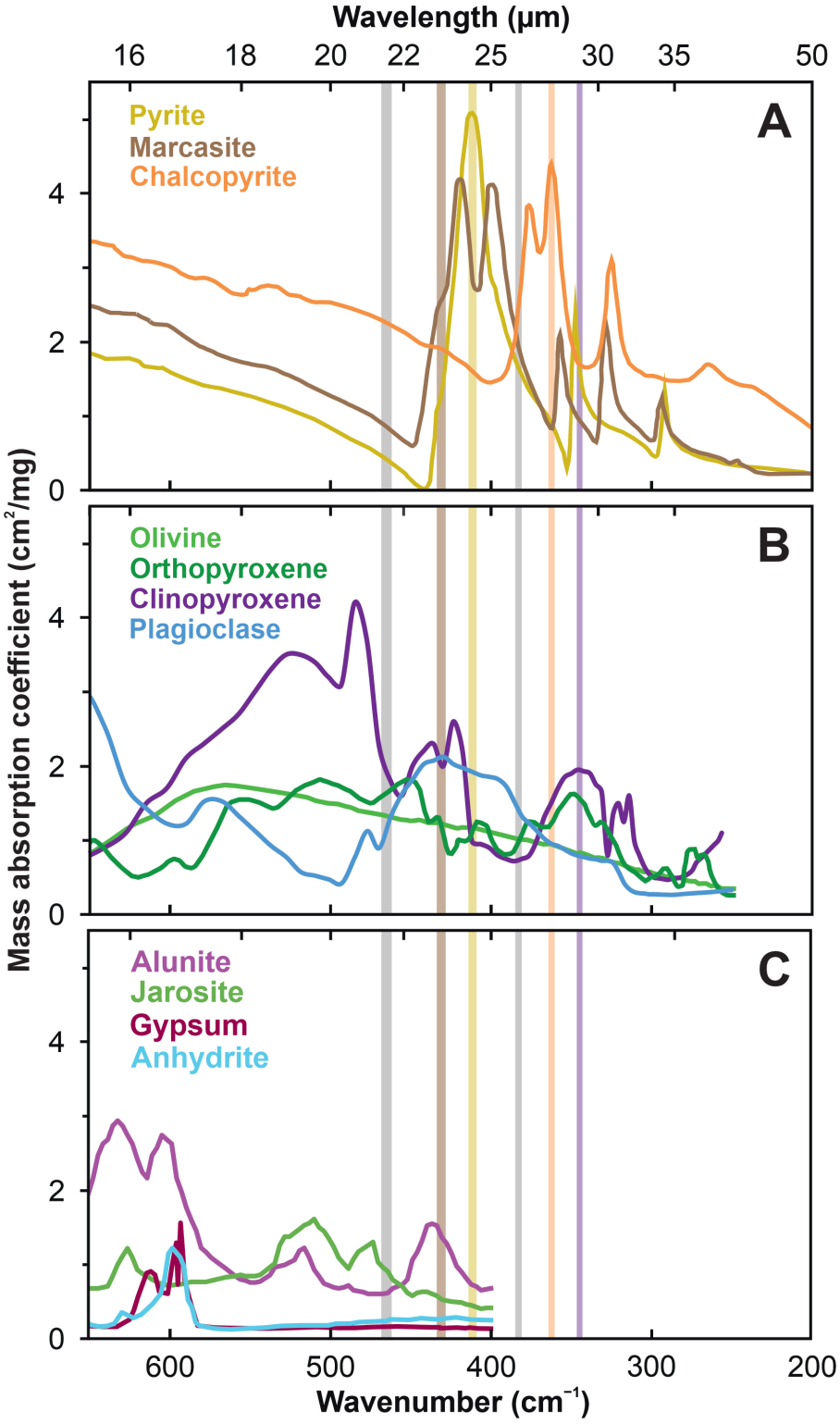

Figure 5. Mass absorption coefficients of possible Martian (**A**) sulfides [23], (**B**) silicates [49–51], and (**C**) sulfates [52–54] measured at room temperature. Literature data for the sulfates and silicates are unavailable for <400 cm^{-1} (>25 μm) and <250 cm^{-1} (>40 μm), respectively. The mass absorption coefficients of sulfates were calculated from reported transmittances, sample masses, and KBr pellet cross-sectional areas according to the method presented by Brusentsova et al. [23]. The spectral ranges of the six detectors are marked with rectangles: orange (360–364 cm^{-1} = 27.45−27.75 μm: chalcopyrite), yellow (409–414 cm^{-1} = 24.15−24.45 μm: pyrite), brown (428–434 cm^{-1} = 23.05−23.35 μm: marcasite), gray (381–385 cm^{-1} = 25.95−26.25 μm and 462–468 cm^{-1} = 21.35−21.65 μm: reference bands), and purple (343–347 cm^{-1} = 28.85−29.15 μm: clinopyroxene).

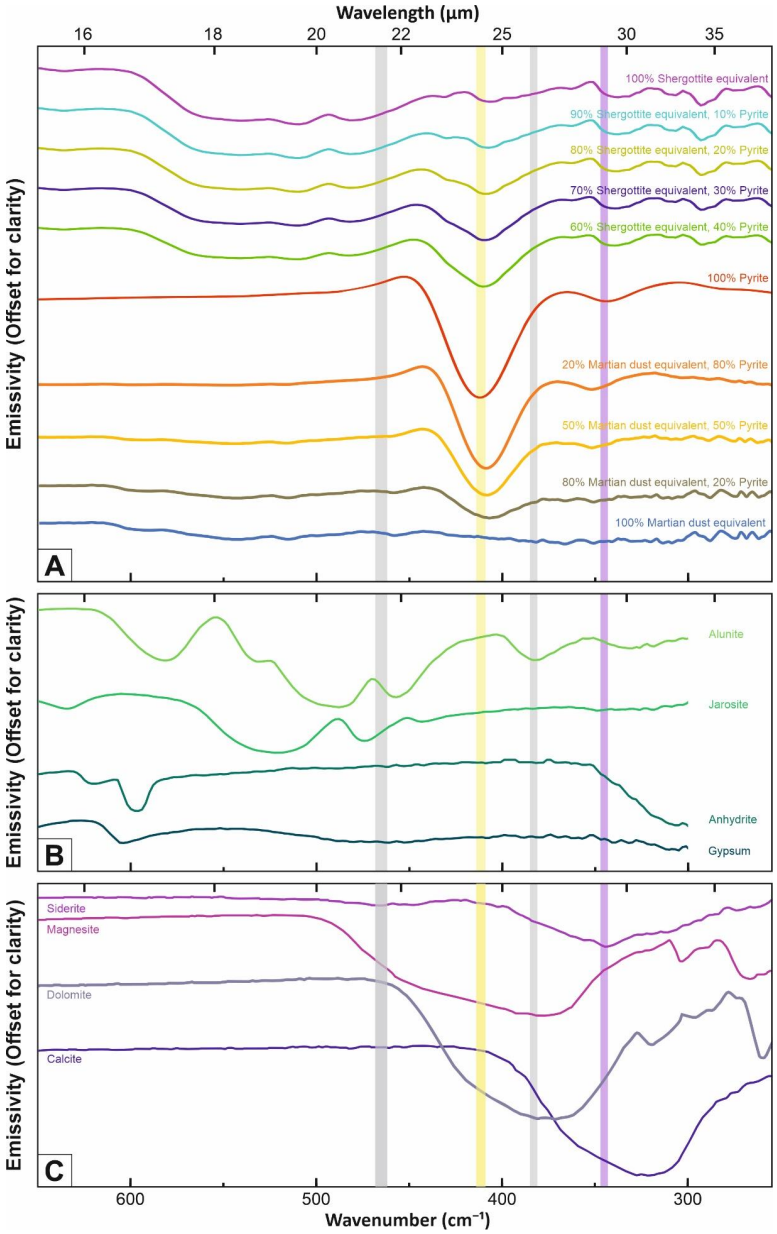

Figure 6. (**A**) presents the emissivity of the Navajún (La Rioja, Spain) pyrite [55], (**B**) equivalents of olivine-phyric shergottites, and (**C**) their various mixtures. The composition of olivine-phyric shergottite equivalents is the same as in the text of Section 3 but normalized from 92% to 100%. The mineral composition of Martian dust is close to JSC Mars-1A (volcanic ash altered at low temperature) proposed by Kölbl et al. [56]: 64% plagioclase (labradorite), 12% olivine (fayalite), 10% magnetite, 9% pyroxene (diopside), and 5% hematite. The input spectra of olivine (fayalite), plagioclase (labradorite), orthopyroxene (bronzite), clinopyroxene (diopside), magnetite, and hematite were collected from the ASU Spectral Library, and was measured by us at the German Aerospace Centre (DLR) in conditions similar to those applied for the ASU measurements: grain dimensions of 710–1000 µm and a surface temperature of 80 °C, but a pressure of 0.7 mbar instead of a nitrogen atmosphere. Emissivity was calibrated against a blackbody measured at the same temperature as the sample. The simulations of various pyrite and shergottite mixtures were performed using the PFSLook software [57]. The spectral ranges of four of the six detectors are marked with the rectangles: yellow (409–414 cm^{-1} = 24.15−24.45 µm: pyrite), grey (381–385 cm^{-1} = 25.95−26.25 µm and 462–468 cm^{-1} = 21.35−21.65 µm: reference bands), and purple (343–347 cm^{-1} = 28.85−29.15 µm: clinopyroxene). Note that the pyrite absorption band becomes visible (under the reference level in grey) when the pyrite content is at least ~20%.

3. Simulated Mass Absorption Coefficients for Various Mineral Mixtures

Large monomineralic fields either on Mars or on Earth are rare and are especially rare for ore minerals. Ore minerals are usually disseminated in host rocks, and emitted spectra would represent a mixture of ore minerals (Figure 5A) and rock-forming minerals (Figure 5B). Whereas the most common ore mineral on Mars is most likely pyrite [11–13,41,58–60], basalts are the most common rocks found by orbiters and in Martian meteorites. To date, >200 distinct meteorites have been classified as samples from Mars. Most of them belong to the SNC clan, which is an abbreviation of shergottites, nakhlites, and chassignites. By far the most abundant of them, shergottites, represent various types of basalts or similar mafic rocks and include three types: most-evolved basaltic, intermediate olivine-phyric, and most-primitive poikilitic. All three types are composed of four minerals in >95 vol.%, i.e., olivine, orthopyroxene, clinopyroxene, and plagioclase, whereas the remaining minerals, including oxides and sulfides, are accessory minerals. The intermediate-type olivine-phyric shergottite is composed of olivine (7–17 vol.%), orthopyroxene (1.5–7.0 vol.%), clinopyroxene (55–65 vol.%), and plagioclase (14–18 vol.%) [21].

Using the linear mixing method, we simulated various mixtures of pyrite and olivine-phyric shergottites (1:9, 2:8, 3:7, 4:6 surface ratios) to determine what would be the minimum amount of pyrite needed to detect it from orbit. Linear mixing of spectra is widely used in various fields of science, from remote sensing through to medicine and biology [61,62]. It has been well-established that thermal infrared spectra of surfaces composed of multiple minerals may be modeled by using linear combinations of each mineral spectrum weighted by the areal fraction of the surface measured [63–65]. Comparison of results obtained by linear mixing and radiative transfer algorithms have shown a good agreement between the two [66,67]. Therefore, emissivities (Figure 6) or mass absorption coefficients measured or incorporated from spectral libraries for single minerals can be combined into the spectrum of a surface using linear mixing. Minerals and their proportions, here, are selected based on the predicted composition of Martian rocks such as basalt and its varieties [68]. For the linear mixing of emissivities (Figure 6), we used the C++-based PFSLook program described by Zalewska and colleagues [57,69]. For mass absorption coefficients (Figure 6), we used our Matlab-based code (see Supplementary Material 3).

We found that fields containing 10–20% pyrite could be detected by the proposed method (Figures 6 and 7). In MIRORES's field of view of 16.5 m × 19.9 m, which makes about ~330 m^2, 33–66 m^2 covered by pyrite will be needed to detect it from orbit. This should allow the detection of not only volcanic-hosted massive sulfide (VMS) deposits but also their stockworks. For example, the Rio Tinto VMS deposits in the Iberian Pyrite Belt contain two large orebodies with massive pyrite, San Dionisio (~600 m × 130 m = 78,000 m^2) and Filon Sur (~1100 m × 50 m = 55,000 m^2), but also larger pyrite stockworks around the Salomon and Argamasilla sites (640 m × 280 m = 179,200 m^2) defined as containing >20% S [70]. This S amount is an equivalent of 23–37 vol.% pyrite, given that pyrite contains 53% S, and has a density of 5.0 g/cm^3, whereas the density of other minerals is between 3–5 g/cm^3. This is considerably more than the 10–20 vol.% needed to detect with MIRORES. Although plate tectonics is currently absent on Mars, it was likely present in the early history of Mars [71,72]. The plate tectonics ceased then but the largest volcanic province, Tharsis, displayed prolonged tectonic activity that was only slowly declining during the Amazonian [73,74]. Therefore, hydrothermal alteration and associated ore deposits are anticipated in the vicinity of volcanic cones, fractures, and degassing structures [75,76]. The largest hydrothermal seafloor deposits documented so far on Mars are 400-m-thick and contain abundant jarosite inferred to form from the oxidation weathering of iron sulfides in the Eridania Basin [77]. The iron sulfides likely formed in a deep-water (500–1500 m) hydrothermal setting. The Eridania basin occurs within some of the most ancient terrains on Mars, where striking evidence for remnant magnetism might suggest an early phase of crustal spreading [77].

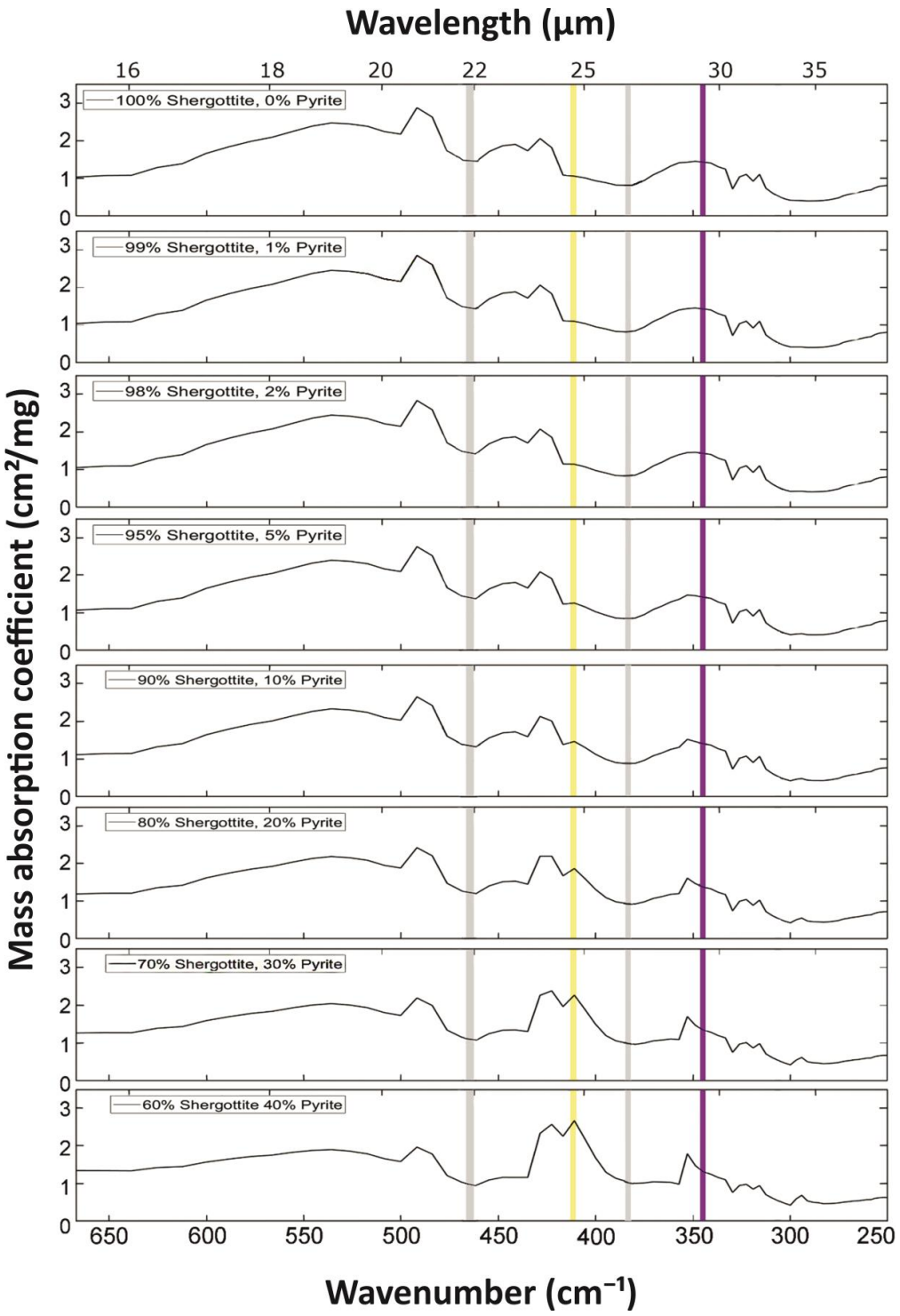

Figure 7. Mass absorption coefficients that we simulated for surfaces composed of various proportions of pyrite and olivine-phyric shergottites. The composition of olivine-phyric shergottites was the same as in the text of Section 3 but normalized from 92% to 100%. The input spectra were derived from Figure 5. The spectral ranges of four of six detectors are marked with rectangles: yellow (409–414 cm^{-1} = 24.15−24.45 μm: pyrite), grey (381–385 cm^{-1} = 25.95−26.25 μm and 462–468 cm^{-1} = 21.35−21.65 μm: reference bands), and purple (343–347 cm^{-1} = 28.85−29.15 μm: clinopyroxene). There is partial interference between pyrite and the secondary clinopyroxene peak on the right (at ~421 cm^{-1} = 23.8 μm, cf. Figure 5), becoming significant when pyrite is <10%. The signal from this interference was taken out using Equation (1). The mineral mixtures were calculated using the Matlab script in Supplementary Material 3.

In impact-related craters >10 km, hydrothermal deposits [78] such as the lenses of massive pyrite may also be large enough to be detected using MIRORES. Large-scale impact-related ore mineralization, although more likely for Mars [10], is also known from several impact craters on Earth such as the Sudbury basin in Canada [79] or the Witwatersrand Supergroup in South Africa [80]. In the Sudbury basin, sulfide ores composed of massive pyrite, such as one located at the Fraser epidote zone, are up to 270 m × 40 m = 10,800 m^2 large [81]. Even larger and also detectable by MIRORES are the local ores of massive chalcopyrite (230 m × 240 m = 55,200 m^2) situated in the West part of the McCreedy East deposit [82]. Note, however, that both the Rio Tinto VMS and impact-related Sudbury deposits contain one of the greatest known concentrations of massive sulfides on Earth [70], so only large or relatively large mineralization can be detected using the MIRORES instrument on Mars.

On Mars, the Gusev, Gale, and other meteorite crater walls are suitable for the remote detection of ore minerals. In the Gusev crater, pyrite and marcasite have been detected by the Mössbauer spectrometer of the Spirit rover, and pyrrhotite was inferred from geochemical constraints [12]. In addition, pyrrhotite was found in two drill powders from the Gale crater analyzed by the Curiosity X-ray diffractometer [13]. These outcrops are not covered by a thin layer of sediments, which could otherwise hinder our measurements, as could potentially larger amounts of dust in the Martian atmosphere during seasonal dust storms. Hydrothermal minerals are preferentially found at crater rims representing products of local impact-induced hydrothermal circulation [10,78]. Other extensive outcrops of hydrothermal deposits are expected to occur in volcanic provinces, where hard rocks are exposed along caldera walls, volcano slopes, and fissures, as demonstrated by Skok et al. [75] and Broz [83] using the CRISM/MRO instrument.

4. General Design

We propose a relatively inexpensive, simple instrument (Figures 8 and 9) measuring only a limited 21–30 μm range of the FIR spectrum, where strong absorption peaks are displayed by most sulfides, including pyrite at 24.3 μm and chalcopyrite at 27.6 μm (Figure 5). In addition, marcasite, with the same chemical composition as pyrite (both FeS_2) but a different crystallographic structure, shows two absorption bands centered close to pyrite (at 25.0 μm and 23.8 μm) and is therefore measured on the short-wave slope of the latter one at 23.2 μm. As well as these three bands, we will measure two bands at 21.5 μm and 26.1 μm for reference (grey bands in Figure 5), which will allow us to interpolate the background level of radiance varying as a function of incidence angle, emission angle, atmospheric H_2O, surface properties, and other factors. Lastly, a special reference detector at 29.0 μm (purple bands in Figure 6) will make it possible to remove partial interference on pyrite from the secondary peak of clinopyroxene at ~24.0 μm by using the following formula:

$$Py_{24.3_{Cpx}} = \frac{Cpx_{29.0} - R_{26.1}}{4} \quad (1)$$

where $Py_{24.3_{Cpx}}$ is the contribution of the secondary peak of clinopyroxene to the absorption peak at the pyrite (Py) detector, $Cpx_{29.0}$ is the signal from the detector monitoring the intensity of the clinopyroxene (Cpx) signal, and $R_{26.1}$ is the signal from the reference detector at 26.1 μm. Here, 0.7 is the ratio between the absorption peak amplitude at the peak of clinopyroxene at 29.0 μm and the absorption peak amplitude of a part of the clinopyroxene ~23.8 μm peak within the pyrite detector. The equation is free of any assumption on the modal content of clinopyroxene on the surface. We only operate on the ratio between the two absorption features of clinopyroxene, which should be relatively constant independent of the clinopyroxene content.

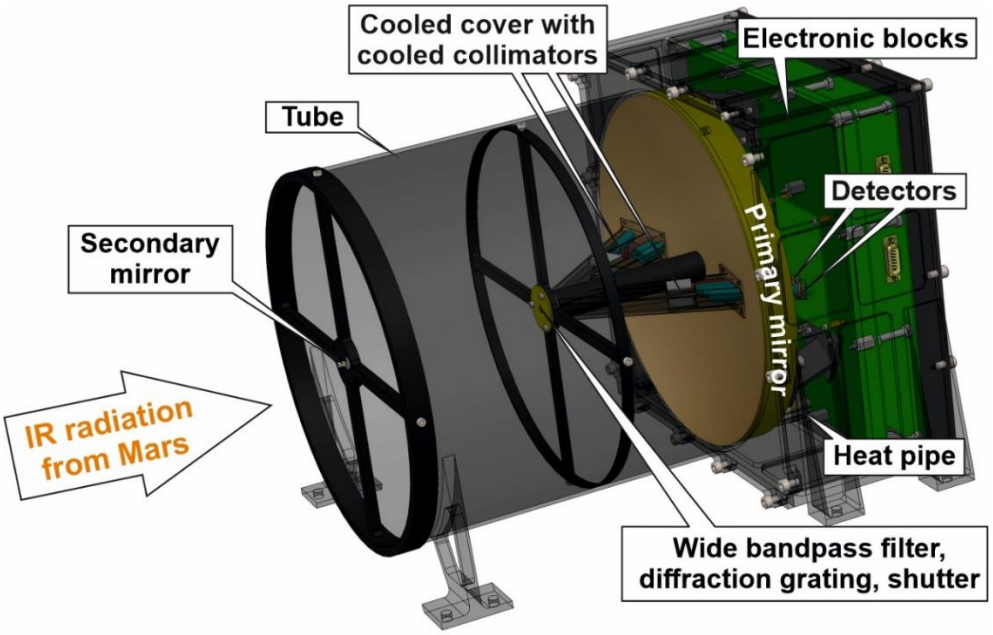

Figure 8. Simplified 3D scheme of the MIRORES instrument. The size of the instrument is 42 × 32 × 32 cm. The spectrometer has seven detectors, two of which are visible on the scheme.

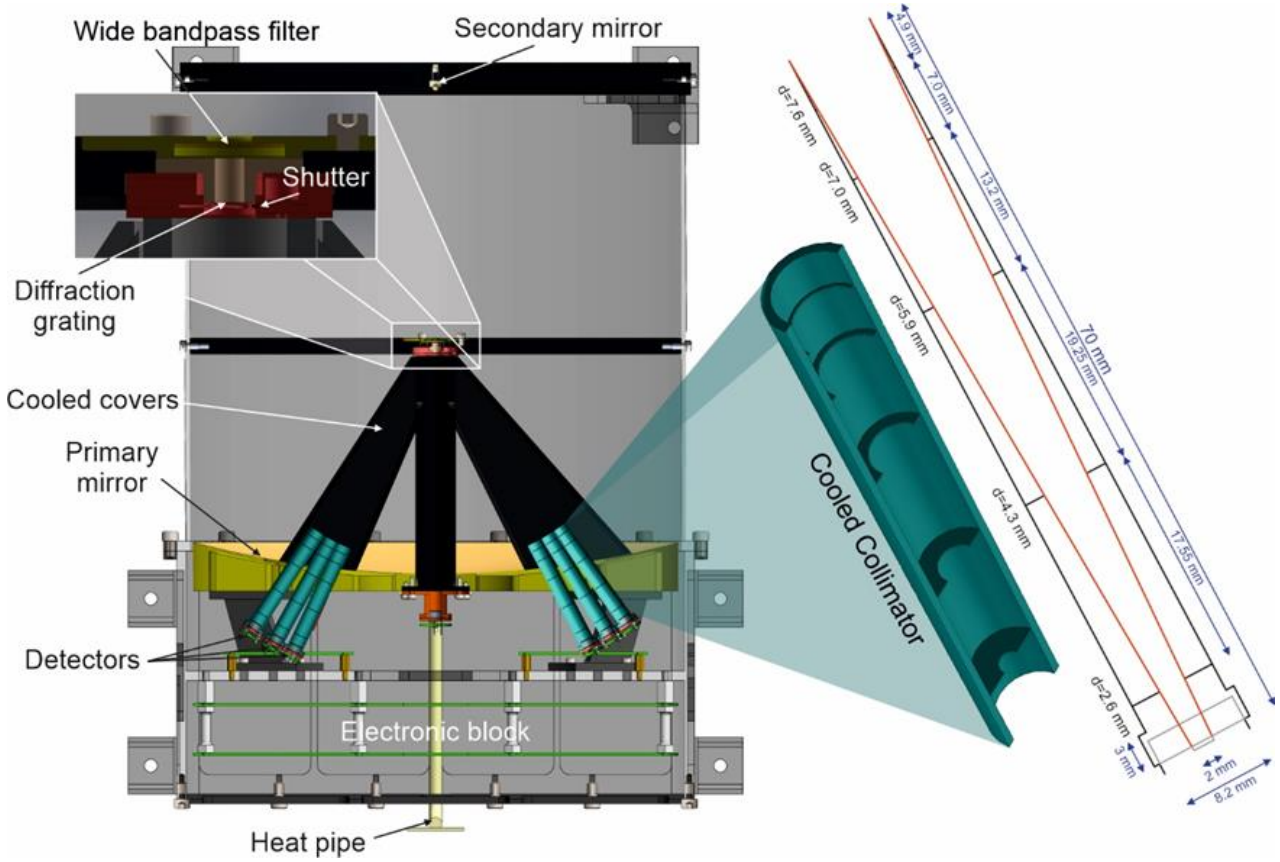

Figure 9. Simplified cross section of the MIRORES instrument. The size of the instrument is 42 × 32 × 32 cm. The six main detectors are placed behind the six turquoise collimators, the optical design of which is depicted on the left. The zoom on the right shows the position of the shutter behind the diffraction grating. The wide bandpass filter transmits radiation in the 21–30 μm range.

Measurements in only six bands allow the instrument dimensions to be 42 × 32 × 32 cm and the instrument mass to be <10 kg (Figures 8 and 9). The instrument optics are based on two mirrors (primary and secondary) set up in a typical Cassegrain system. The primary mirror with a diameter of 300 mm reflects the radiation into the smaller secondary mirror with a diameter of 4.1 mm located at a distance of 300 mm. Then, all radiation reflected from the secondary mirror is directed to the wide bandpass filter (20−33 μm) and a diffraction grating. Here, the broadband beam is split into six quasi-monochromatic beams, which are refracted and fall into the set of six pyroelectric detectors (three for target minerals, two for reference, and one for the clinopyroxene interference). The detectors are mounted on a copper plate to facilitate heat dissipation. Heat dissipation is reinforced by a temperature stabilization system. The radiation stream transmitted by the device's optical system is digitized by a front-end electronics (FEE) system and sent to an onboard computer.

The key components of the instrument, the primary and secondary mirrors, will be connected to the satellite through heat pipes. Assuming that the mirrors are shielded from direct solar radiation by the satellite body, they receive only from 22 W (Mars blackbody radiation) to 32 W (blackbody radiation + reflected radiation from the Sun), so the heat pipes need to expel on average 27 W to maintain a constant temperature. In the assumed model, Mars has a temperature of 193 K at night, the solar flux is 715 W/m^2, the satellite temperature is 273 K, the space temperature is 4 K, and the electronic power dissipates up to 10 W.

5. Optical System

The optical system is composed of a primary mirror, a secondary mirror, a filter, a diffraction grating, and collimators for each detector (Figure 9). The primary mirror has a diameter of 300 mm and is made of alumina. The secondary mirror is formed by a gold-covered steel sphere; which is a bearing ball with a diameter of 4.1 mm easily available on the market, manufactured, for example, by FŁT Polska Sp. Z.o.o. The distance between the primary and secondary mirrors is 300 mm (Figure 10). The effective focal length of the telescope is 30.3 m, the detector window diameter is 2 mm, and the assumed satellite altitude is 250 km. The field of view in a static position can thus be calculated as 0.002 m through 30.3 m times 250,000 m, which makes 16.5 m. Given that the satellite will move during the 1 ms measurement with an orbital speed of 3430 m/s, the shift related to the satellite position change is 3.4 m. Therefore, the length of the field of view along the satellite path will be 19.9 m, so the field of view can be reported as 16.5 m × 19.9 m (328.4 m^2). This field resolution should correspond to an angular resolution of $6.6 \cdot 10^{-5}$ radians, which equals 13.6 arcsecs. This translates to an F-number of 101 (see also Supplementary Figure S2 in Supplementary Material 1). This value, although high, is sufficient for our spectrometer measuring just one spectrum at a given time. Therefore, this amount of light is sufficient to obtain proper results above the noise level.

The light reflected from the secondary mirror goes through the wide bandpass multilayer interference temperature-invariant filter (Figure 9) made of chemical vapor deposition diamond. Thanks to pre-coating with amorphous hydrogenated diamond-like carbon (DLC) and coating with multilayers of ZnSe and PbTe, the filter can cut off the visible, as well as near-, and mid-infrared radiation (<20 μm), as well as radiation >33 μm [84]. The filtered light, including the useful spectral range (21–30 μm), then goes through the transmission diffraction grating with a pitch of 50 μm made of aluminum frame and 25-micrometer-thick copper wire. These parameters allow us to obtain a spectral resolution of ~0.3 μm. For example, the spectral resolution for the 21.5 μm detector is 0.31 μm, calculated as 21.5 μm through 70 (number of active slits, 20 active slits/1 mm).

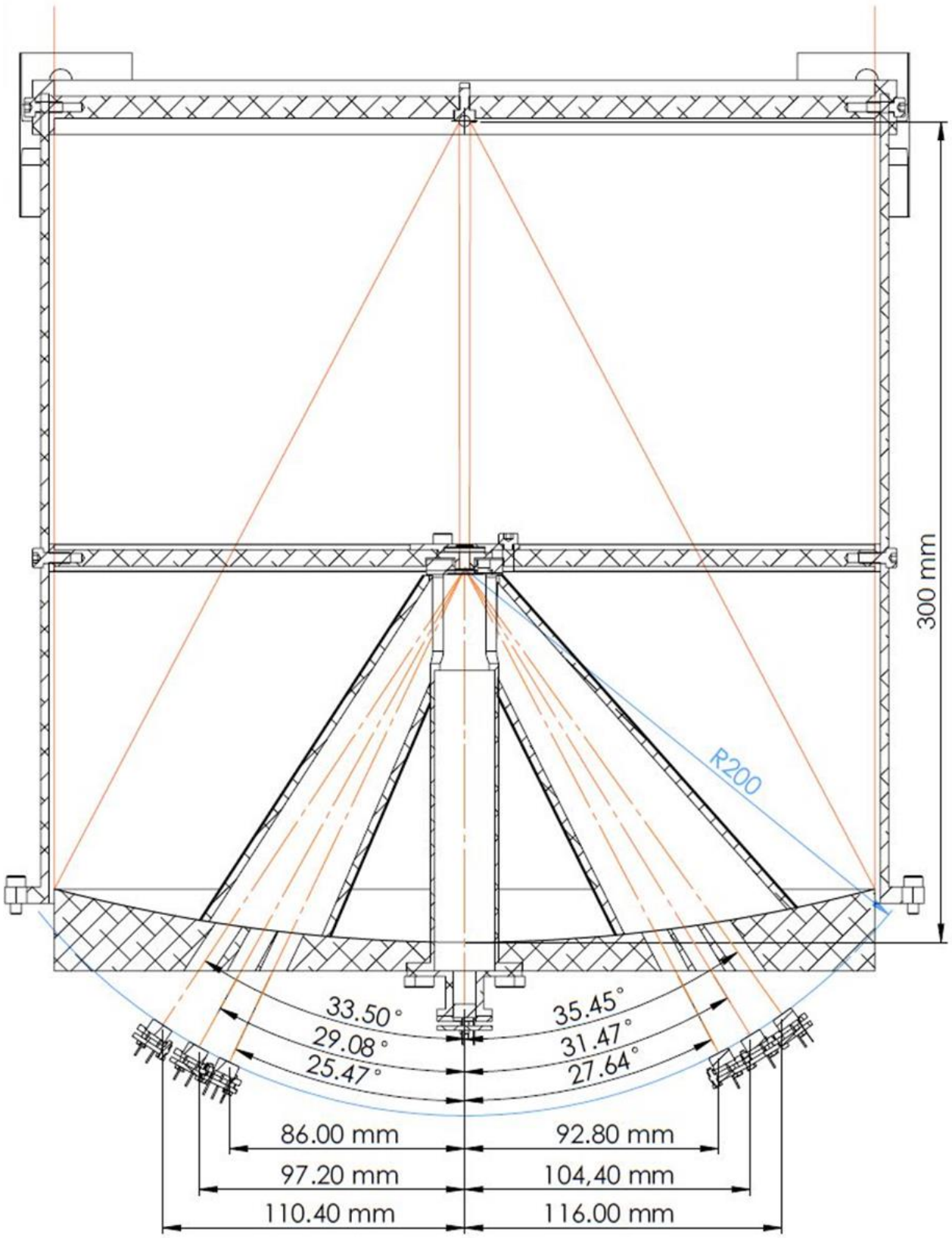

Figure 10. The optical system of the MIRORES instrument with the primary mirror at the bottom, and the secondary mirror at the top. Orange solid lines: incident radiation; orange dash–dotted lines: refracted radiation. R200 is the distance between the detectors and diffraction grating (200 mm). The thin blue curve marks this distance of 200 mm from the diffraction grating, and all the detectors are situated along this theoretical curve.

The distance from the diffraction grating to each detector is 200 mm. The light passing through the diffraction grating is refracted with an angle (θ) that can be calculated from the following formula Equation (2):

$$\lambda = \frac{p \times \sin\theta}{n} \quad (2)$$

where λ is the refracted wavelength, p is the pitch of the diffraction grating, and n is the refraction order. In our case, the refraction order is always 1 as wavelengths of <20 µm, distinguished by higher radiation levels, are filtered out. The radiation in the third order, which is always cut off by the filter, would be nine times weaker. The radiation in the second order would be four times weaker but the even orders are neutralized in this optical geometry.

The positions of the three main detectors and three reference detectors (Figure 10) are calculated from the refraction angle and the distance between detectors and diffraction grating (200 mm). These positions are + 116.00 mm ($Cpx_{29.0}$), + 104.40 mm ($R_{26.1}$), + 92.80 mm (marcasite at 23.2 µm − $Mrc_{23.2}$), −86.00 mm ($R_{21.5}$), −97.20 mm ($Py_{24.3}$), and −110.40 mm (chalcopyrite at 27.6 µm − $Ccp_{27.6}$) from the optical axis (Figure 8). All detectors register radiation from the same area of Mars. The non-refracted portion of radiation travels straight to the seventh detector located at position 0 (Figure 10). This detector registers the broadband non-refracted radiation >20 µm to monitor the brightness of the Martian surface. In the optical axis, the sizes of the light beams on the detectors are 3.4 mm, which are a bit larger than the size of the detector apertures (2 mm) but smaller than the size of the Airy disc (corresponding to the first minimum of the Airy pattern). The quality of the beam is relatively insensitive to potential change in the position of the focal plane (see Supplementary Figure S3 in Supplementary Material 1). Predicted mechanical deformation due to estimated temperature changes (Supplementary Figure S4 in Supplementary Material 1) should not affect the quality of the optical system (Supplementary Figure S2 in Supplementary Material 1). The full ray-tracing analysis and tolerance analysis are included in Supplementary Material 1 (Supplementary Figures S2 and S5, respectively). The light paths in the section between the diffraction grating and detectors are surrounded by the PA 2200 powdered polyamide cover to protect the detectors against potential stray light (Figure 8).

The position of the detectors may change slightly after future tests and calibrations, but this will not be significant. For example, pyrite, which is the most important in our set of minerals, is planned to be measured at 411.5 cm^{-1} (24.3 µm) following the values reported in our emissivity measurements (Figure 6); however, Brusentova et al. [23] indicated 412 cm^{-1} (24.3 µm) and Farmer [30] reported 415 cm^{-1} (24.1 µm). These values are further supported by other numerous studies [24–26] with the one exception of Lennie and Vaughan [85], who reported 425 cm^{-1} (23.5 µm). The purpose of that study was, however, related to the phase transition between pyrite and marcasite, and its spectroscopy results were only intended to identify phases. Therefore, the authors needed only qualitative or semiquantitative spectral features of the minerals with no need for high accuracy of the measurements. More problematic could be the fact that the wavenumber of spectral features increases with decreasing temperatures, which, according to Farmer [30], is ~0.1 $cm^{-1}/°C$ for some bonds such as O–H. This rate is, however, at least one order of magnitude lower for most Fe–S bonds crucial for sulfide detection [23].

6. Detection System

The detection system consists of six infrared-sensitive optoelectronic components based on the L3100 × 2020 detectors provided by Laser Components GMBH (Figure 11). These are pyroelectric detectors operating with a single voltage supply (VCC). The detector specific sensitivity (D *) expressed in Jones units is ~9×10^8 $cmHz^{1/2}/W$ at 10 Hz. The signal to noise ratio is >2 (for 1 ms). The output signal after digitalization in FEE is 16 bits (Supplementary Materials 4 and 5) and the required data rate volume is the basic standard of 115,000 b/s assuming that one measurement lasts 1 ms and measurement occurs every

5.59 ms. The collected signal can also be temporarily stored on an onboard computer mounted in the electronic blocks (Figure 8).

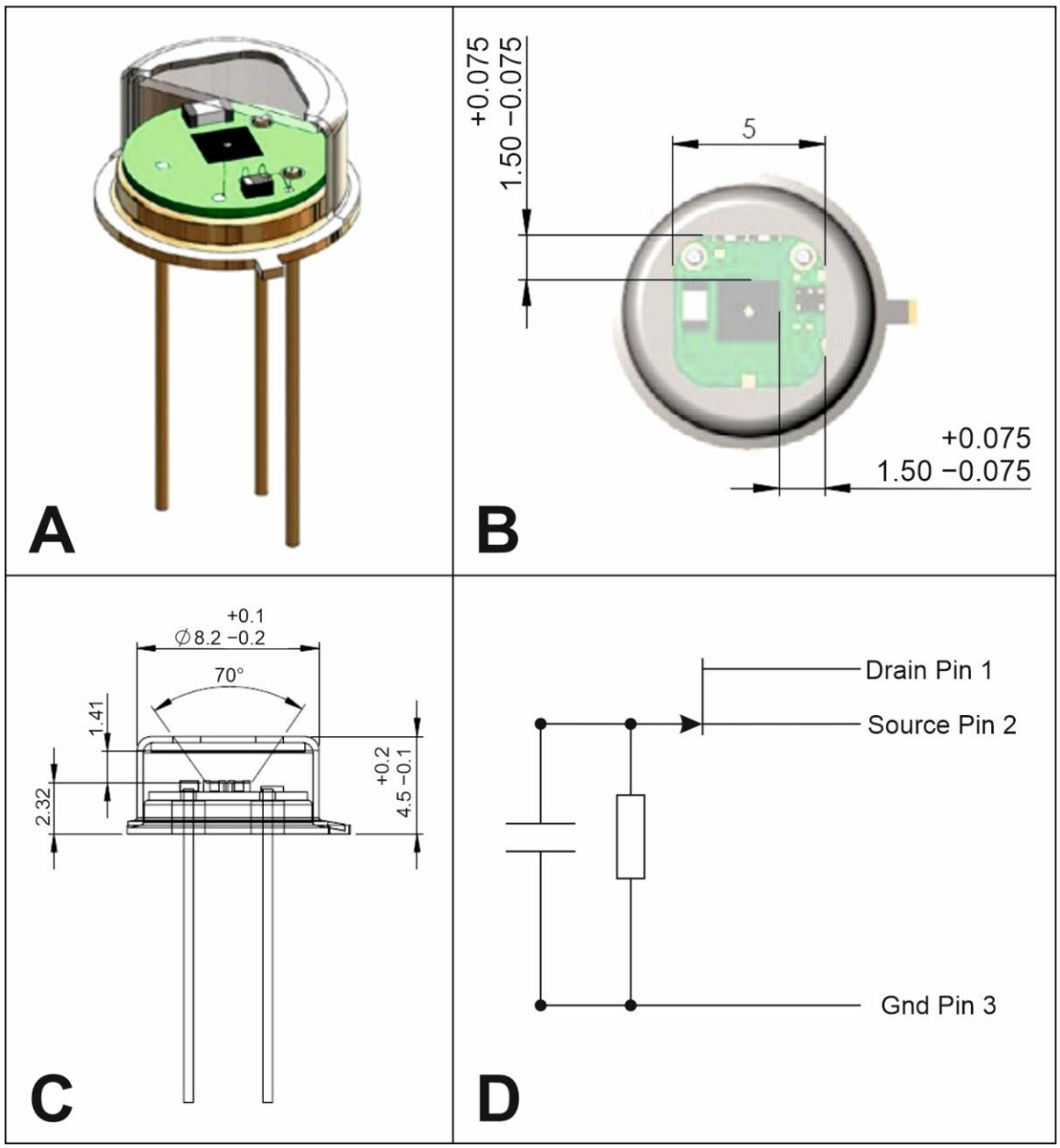

Figure 11. (**A**) Three-dimensional cross section of pyroelectric detector L3100 × 2020, followed by its horizontal (**B**) and vertical (**C**) cross sections. All reported distances are in mm. (**D**) Circuit diagram of the detector.

As pyroelectric detectors are sensitive only to modulated radiation, we mounted a shutter behind the wide bandpass filter and the diffraction grating (Figure 9). The detectors show high transmission (>60%) of the far-infrared radiation (>15 µm) and low transmission (0–40%) of the mid- and near-infrared (<15 µm). The detector has a built-in high-density polyethylene (HDPE) filter. To protect the detectors, we also need additional filters to cut out more radiation <20 µm, including potentially damaging UV radiation. Although one such filter for the incoming radiation is located in front of the diffraction grating, additional filters are needed in front of each detector to eliminate thermal radiation from all the components placed between the primary filter and the detectors, such as the primary mirror or collimators.

For the Mars temperature of 293 K and surface emissivity of 1, we obtain a heat of $2.45 \cdot 10^{-9}$ W at the detector (calculated for the pyrite detector receiving radiation from 24.15−24.45 μm) assuming no loss of signal on the filters and diffraction grating. In reality, our wideband pass filter, which is not cooled, transmits only ~85% radiation at this band, and the cooled narrowband filter passes 90% of the radiation. Considering that another 50% of radiation is lost on the diffraction grating and 7% is lost on around the detector due to the difference between the area of the beam (diameter of 3.5 mm), and aperture of the detector (square 2 × 2 mm) assuming Gaussian distribution of radiation intensity within the beam, the entire loss is 100% – (90% × 85% × 50% × 93%) = 64%. Therefore, the true signal is $0.82 \cdot 10^{-9}$ W. This, after amplification of 10,000 V/W, becomes 8.2 μV. The noise is calculated based on radiation from parts of collimators directly visible from a detector (40 mm^2 translating to 1 mm^2 when considering the angle between the collimator and detector planes) and their temperature (50 K). Given that each detector is shielded with a narrow bandpass filter, which is 23.4−25.2 μm for the pyrite detector, we obtain a value of $0.58 \cdot 10^{-9}$ W and $0.52 \cdot 10^{-9}$ W considering the filter transmission of 90%, which becomes 5.2 μV after signal amplification. With 8.2 μV obtained for the signal and 5.2 μV obtained for the noise, the calculated signal to noise ratio is 1.6. One cooling system that can be potentially applied to cool the detectors and parts of collimators (the 40 mm^2) in view of the detectors, to stabilize the instrument background and simplify the in-flight radiometric calibration, is used by Rigopoulou et al. [86]. The rest of collimator and the cover (Figure 8) are cooled to 190 K with a Peltier system and heatpipe.

For radiance calibration, we will observe two sources at known temperatures, deep space and an external plate mounted on the satellite. Deep space is characterized by a constant temperature and will be measured at least twice per orbit. The plate will be measured every 10 min and will have variable but known temperatures that can be measured continously with an expected accuracy of 0.1 K.

7. Conclusions

At least three common hydrothermal sulfides on Earth and Mars (pyrite, chalcopyrite, marcasite) have prominent absorption peaks in a narrow far-IR (FIR) wavelength range of 23–28 μm. The spectral features of sulfides in the FIR range are much stronger than the spectral features of any of the common Martian minerals, including olivines, clinopyroxenes, orthopyroxenes, plagioclase, major sulfates and major carbonates. Our simulations indicated that fields containing 10–20% pyrite could be detected from orbit in the far-IR range. However, ore deposits including massive pyrite are relatively small, maximally up to hundreds of meters by hundreds of meters. Therefore, although the existing instruments PFS/MEX and TES/MGS cover the FIR spectral range, their spatial resolutions of ~10 km and ~3 km, respectively, are not sufficient to search for ore deposits.

Therefore, we designed a new instrument with a resolution that allows detecting ore deposits. This was achieved by the use of the Cassegrain optical system. The field of view of 16.5 × 19.9 m makes it possible to detect areas covered by 33–66 m^2 of pyrite on a surface of ~330 m^2, creating possibilities for detecting large and moderate-size orebodies and probably also their stockworks. The instrument should be integrated into a satellite launched to Mars, such as that planned by the Polish mission to Mars consortium or a larger mission between 2026 and 2030, the Earth Return Orbiter of ESA in 2026/28 or the Mars Sample Return mission (HX-2) of the China National Space Administration (CNSA) in 2028/30. Prototype creation was started in 2021 and prototype testing is scheduled for 2022–2024.

Supplementary Materials: The following supporting information can be downloaded at: https://www.mdpi.com/article/10.3390/rs14122799/s1. References [23,87–91] are cited in the supplementary materials.

Author Contributions: Conceptualization, J.C., J.B. (Jaroslaw Bakala), M.K. (Miroslaw Kowalinski), S.P., M.C., J.B. (Jaromir Barylak) and M.R.; Investigation, N.Z., G.P., M.S., J.B. (Jaromir Barylak), M.K. (Mateusz Kuzaj), A.M. (Alessandro Maturilli) and J.H.; Methodology, J.C., J.B. (Jaroslaw Bakala), M.K. (Miroslaw Kowalinski), S.P., N.Z., G.P., A.M. (Alessandro Maturilli) and J.H.; Project administration, M.J.; Resources, N.Z.; Software, S.P., N.Z. and M.S.; Supervision, J.C. and M.K. (Miroslaw Kowalinski); Visualization, J.B. (Jaroslaw Bakala), M.K. (Miroslaw Kowalinski), N.Z., B.P., M.C., G.P., M.S. and M.K. (Mateusz Kuzaj); Writing — original draft, J.C., M.K. (Miroslaw Kowalinski), S.P. and N.Z.; Writing — review & editing, J.C., J.B. (Jaroslaw Bakala), M.K. (Miroslaw Kow-alinski), S.P., N.Z., B.P., T.M., M.C., M.S., Z.S., A.M. (Andrzej Muszynski), S.G., M.J. and D.M. All authors have read and agreed to the published version of the manuscript.

Funding: The work was funded by the NCN project no. 2020/37/B/ST10/01420 to J. Ciazela, the European Space Agency (ESA) Space Resources project no. ESA AO/1-10824/21/NL/RA, and the European Funds Smart Growth (PO WER) project no. POWR.03.02.00-00-I027/17.

Data Availability Statement: Supplementary Materials 1–5 are available online.

Conflicts of Interest: The authors declare no conflict of interest.

References

1. Messina, P.; Vennemann, D. The European space exploration programme: Current status of ESA's plans for Moon and Mars exploration. *Acta Astronaut.* **2005**, *57*, 156–160. [CrossRef] [PubMed]
2. International Space Exploration Coordination Group. *The Global Exploration Roadmap*; National Aeronautics and Space Administration: Washington, DC, USA, 2013.
3. International Space Exploration Coordination Group. *The Global Exploration Roadmap*; National Aeronautics and Space Administration: Washington, DC, USA, 2018.
4. European Space Agency (ESA). ESA Space Resources Strategy. Available online: https://sci.esa.int/documents/34161/35992/1567260390250-ESA_Space_Resources_Strategy.pdf (accessed on 22 May 2019).
5. U.S. Geological Survey. *Mineral Commodity Summaries*; Online; U.S. Geological Survey: Washington, DC, USA, 2016.
6. Vaughan, D.J.; Corkhill, C.L. Mineralogy of sulfides. *Elements* **2017**, *13*, 81–87. [CrossRef]
7. King, P.L.; McSween, J.Y. Effects of H_2O, pH, and oxidation state on the stability of Fe minerals on Mars. *J. Geophys. Res. E Planets* **2005**, *110*, 113. [CrossRef]
8. King, P.L.; McLennan, S.M. Sulfur on Mars. *Elements* **2010**, *6*, 107–112. [CrossRef]
9. Pirajno, F.; van Kranendonk, M.J. Review of hydrothermal processes and systems on Earth and implications for Martian analogues. *Aust. J. Earth Sci.* **2005**, *52*, 329–351. [CrossRef]
10. West, M.D.; Clarke, J.D.A. Potential martian mineral resources: Mechanisms and terrestrial analogues. *Planet. Space Sci.* **2010**, *58*, 574–582. [CrossRef]
11. Squyres, S.W.; Aharonson, O.; Clark, B.C.; Cohen, B.A.; Crumpler, L.; De Souza, P.A.; Farrand, W.H.; Gellert, R.; Grant, J.; Grotzinger, J.P.; et al. Pyroclastic activity at home plate in Gusev crater, Mars. *Science* **2007**, *316*, 738–742. [CrossRef]
12. Morris, R.V.; Klingelhöfer, G.; Schröer, C.; Fleischer, I.; Ming, D.W.; Yen, A.S.; Gellert, R.; Arvidson, R.E.; Rodionov, D.S.; Crumpler, L.S.; et al. Iron mineralogy and aqueous alteration from Husband Hill through Home Plate at Gusev Crater, Mars: Results from the Mössbauer instrument on the Spirit Mars Exploration Rover. *J. Geophys. Res. E Planets* **2008**, *113*, E12S42. [CrossRef]
13. Vaniman, D.T.; Bish, D.L.; Ming, D.W.; Bristow, T.F.; Morris, R.V.; Blake, D.F. Mineralogy of a Mudstone at Bay, Yellowknife Crater, Gale. *Science* **2014**, *343*, 1–9. [CrossRef]
14. Wang, Z.; Becker, H. Chalcophile elements in Martian meteorites indicate low sulfur content in the Martian interior and a volatile element-depleted late veneer. *Earth Planet. Sci. Lett.* **2017**, *463*, 56–68. [CrossRef]
15. Wang, Z.; Becker, H. Silver contents and Cu/Ag ratios in Martian meteorites and the implications for planetary differentiation. *Geochim. Cosmochim. Acta* **2017**, *216*, 96–114. [CrossRef]
16. Baumgartner, R.J.; Fiorentini, M.L.; Lorand, J.P.; Baratoux, D.; Zaccarini, F.; Ferrière, L.; Prašek, M.K.; Sener, K. The role of sulfides in the fractionation of highly siderophile and chalcophile elements during the formation of martian shergottite meteorites. *Geochim. Cosmochim. Acta* **2017**, *210*, 1–24. [CrossRef]
17. Lorand, J.P.; Pont, S.; Chevrier, V.; Luguet, A.; Zanda, B.; Hewins, R. Petrogenesis of martian sulfides in the Chassigny meteorite. *Am. Mineral.* **2018**, *103*, 872–885. [CrossRef]
18. Franz, H.B.; Kim, S.T.; Farquhar, J.; Day, J.M.D.; Economos, R.C.; McKeegan, K.D.; Schmitt, A.K.; Irving, A.J.; Hoek, J.; Iii, J.D. Isotopic links between atmospheric chemistry and the deep sulphur cycle on Mars. *Nature* **2014**, *508*, 364–368. [CrossRef]
19. Bibring, J.-P.; Soufflot, A.; Berthe, M.; All, E. OMEGA: Observatoire pour la Mineralogie, I'Eau, les Glaces et I'Activite. *Mars Express Sci. Payload* **2004**, *1240*, 37–49.
20. Horgan, B.H.N.; Cloutis, E.A.; Mann, P.; Bell, J.F. Near-infrared spectra of ferrous mineral mixtures and methods for their identification in planetary surface spectra. *Icarus* **2014**, *234*, 132–154. [CrossRef]

21. Taylor, L.A.; Nazarov, M.A.; Shearer, C.K.; McSween, H.Y.; Cahili, J.; Neal, C.R.; Ivanova, M.A.; Barsukova, L.D.; Lentz, R.C.; Clayton, R.N.; et al. Martian meteorite Dhofar 019: A new shergottite. *Meteorit. Planet. Sci.* **2002**, *37*, 1107–1128. [CrossRef]
22. Bibring, J.P.; Langevin, Y.; Mustard, J.F.; Poulet, F.; Arvidson, R.; Gendrin, A.; Gondet, B.; Mangold, N.; Pinet, P.; Forget, F.; et al. Global mineralogical and aqueous Mars history derived from OMEGA/Mars express data. *Science* **2006**, *312*, 400–404. [CrossRef]
23. Brusentsova, T.; Peale, R.E.; Maukonen, D.; Figueiredo, P.; Harlow, G.E.; Ebel, D.S.; Nissinboim, A.; Sherman, K.; Lisse, C.M. Laboratory far-infrared spectroscopy of terrestrial sulphides to support analysis of cosmic dust spectra. *Mon. Not. R. Astron. Soc.* **2012**, *420*, 2569–2579. [CrossRef]
24. Hony, S.; Bouwman, J.; Keller, L.P.; Waters, L.B.F.M. The detection of iron sulfides in Planetary Nebulae. *Astron. Astrophys.* **2003**, *393*, L103–L106. [CrossRef]
25. Dyar, M.D.; Holden, P.; Bishop, J.L.; Lane, M.D. Spectroscopic Characterization of hydrothermal sulfide chimneys at the Juan de Fuca Ridge. *Lunar Planet. Sci. Conf.* **2009**, *40*, 2221.
26. Nian-Xin, M.; Ye-Xiao, H.; Wei, L.; Hong-Juan, Y.; Xue-Chu, S. Far-infrared spectra of naturally occuring FeS2 (Pyrite). *Acta Phys. Sin.* **1993**, *42*, 1712–1718. [CrossRef]
27. Lorand, J.P.; Chevrier, V.; Sautter, V. Sulfide mineralogy and redox conditions in some shergottites. *Meteorit. Planet. Sci.* **2005**, *40*, 1257–1272. [CrossRef]
28. Gattacceca, J.; Hewins, R.H.; Lorand, J.P.; Rochette, P.; Lagroix, F.; Cournède, C.; Uehara, M.; Pont, S.; Sautter, V.; Scorzelli, R.B.; et al. Opaque minerals, magnetic properties, and paleomagnetism of the Tissint Martian meteorite. *Meteorit. Planet. Sci.* **2013**, *48*, 1919–1936. [CrossRef]
29. Smith, M.R.; Bandfield, J.L. Geology of quartz and hydrated silica-bearing deposits near Antoniadi Crater, Mars. *J. Geophys. Res. Planets* **2012**, *117*, 34. [CrossRef]
30. Farmer, V.C. *Infrared Spectra of Minerals*; Mineralogical Society: London, UK, 1974.
31. Rogalski, A. Next decade in infrared detectors. In Proceedings of the Electro-Optical and Infrared Systems: Technology and Applications XIV. International Society for Optics and Photonics, Warsaw, Poland, 9 October 2017; Volume XIV, p. 104330L. [CrossRef]
32. Safari, M.; Maghsoudi, A.; Pour, A.B. Application of Landsat-8 and ASTER satellite remote sensing data for porphyry copper exploration: A case study from Shahr-e-Babak, Kerman, south of Iran. *Geocarto Int.* **2018**, *33*, 1186–1201. [CrossRef]
33. Read, P.L.; Lewis, S.R.; Mulholland, D.P. The physics of Martian weather and climate: A review. *Rep. Prog. Phys.* **2015**, *78*, 125901. [CrossRef]
34. Montabone, L.; Forget, F.; Millour, E.; Wilson, R.J.; Lewis, S.R.; Cantor, B.; Kass, D.; Kleinböhl, A.; Lemmon, M.T.; Smith, M.D.; et al. Eight-year climatology of dust optical depth on Mars. *Icarus* **2015**, *251*, 65–95. [CrossRef]
35. Bandfield, J.L. Global mineral distributions on Mars. *J. Geophys. Res.* **2002**, *107*, 5042. [CrossRef]
36. Farrand, W.H.; Glotch, T.D.; Rice, J.W.; Hurowitz, J.A.; Swayze, G.A. Discovery of jarosite within the Mawrth Vallis region of Mars: Implications for the geologic history of the region. *Icarus* **2009**, *204*, 478–488. [CrossRef]
37. Zalewska, N. Hellas Planitia as a potential site of sedimentary minerals. *Planet. Space Sci.* **2013**, *78*, 25–32. [CrossRef]
38. Chukanov, N.V.; Chervonnyi, A.D. *Infrared Spectroscopy of Minerals and Related Compounds*; Springer: Cham, Switzerland, 2016; ISBN 3319253492.
39. Carter, J.; Viviano-Beck, C.; Loizeau, D.; Bishop, J.; Le Deit, L. Orbital detection and implications of akaganéite on Mars. *Icarus* **2015**, *253*, 296–310. [CrossRef]
40. Bajda, T. Solubility of mimetite Pb5(AsO4)3Cl at 555C. *Environ. Chem.* **2010**, *7*, 268–278. [CrossRef]
41. Ehlmann, B.L.; Edwards, C.S. Mineralogy of the Martian Surface. *Annu. Rev. Earth Planet. Sci.* **2014**, *42*, 291–315. [CrossRef]
42. Cousin, A.; Sautter, V.; Payré, V.; Forni, O.; Mangold, N.; Gasnault, O.; Le Deit, L.; Johnson, J.; Maurice, S.; Salvatore, M.; et al. Classification of igneous rocks analyzed by ChemCam at Gale crater, Mars. *Icarus* **2017**, *288*, 265–283. [CrossRef]
43. Xue, Y.; Yang, Y.; Yu, L. Mineral composition of the Martian Gale and Nili Fossae regions from Mars Reconnaissance Orbiter CRISM images. *Planet. Space Sci.* **2018**, *163*, 97–105. [CrossRef]
44. Singh, P.; Sarkar, R.; Porwal, A. Orbital remote sensing of impact-induced hydrothermal systems on Mars. *Ore Geol. Rev.* **2019**, *108*, 101–111. [CrossRef]
45. Mancarella, F.; Fonti, S.; Alemanno, G.; Orofino, V.; Blanco, A. Aqueous alteration detection in Tikhonravov crater, Mars. *Planet. Space Sci.* **2018**, *152*, 165–175. [CrossRef]
46. Lin, H.; Zhang, X. Retrieving the hydrous minerals on Mars by sparse unmixing and the Hapke model using MRO/CRISM data. *Icarus* **2017**, *288*, 160–171. [CrossRef]
47. Bandfield, J.L.; Glotch, T.D.; Christensen, P.R. Spectroscopic identification of carbonate minerals in the martian dust. *Science* **2003**, *301*, 1084–1087. [CrossRef]
48. Rothman, L.S.; Gordon, I.E.; Babikov, Y.; Barbe, A.; Benner, D.C.; Bernath, P.F.; Birk, M.; Bizzocchi, L.; Boudon, V.; Brown, L.R.; et al. The HITRAN2012 molecular spectroscopic database. *J. Quant. Spectrosc. Radiat. Transf. HITRAN2012 Mol. Spectrosc. Database* **2013**, *130*, 4–50. [CrossRef]
49. Gielen, C.; Van Winckel, H.; Min, M.; Waters, L.; Evans, T.L. SPITZER survey of dust grain processing in stable discs around binary post-AGB stars. *Astron. Astrophys.* **2008**, *490*, 725–735. [CrossRef]
50. Koike, C.; Tsuchiyama, A.; Shibai, H.; Suto, H.; Tanabé, T.; Chihara, H.; Sogawa, H.; Mouri, H.; Okada, K. Absorption spectra of Mg-rich Mg-Fe and Ca pyroxenes in the mid- and far-infrared regions. *Astron. Astrophys.* **2000**, *363*, 1115–1122.

51. Chihara, H.; Koike, C. Infrared absorption spectra of plagioclase feldspar: Dependencies of composition and temperature. *Planet. Space Sci.* **2017**, *149*, 94–99. [CrossRef]
52. Bishop, J.; Murad, E. The visible and infrared spectral properties of jarosite and alunite. *Am. Mineral.* **2005**, *90*, 1100–1107. [CrossRef]
53. Bishop, J.L.; Lane, M.D.; Dyar, M.D.; King, S.J.; Brown, A.J.; Swayze, G.A. Spectral properties of Ca-sulfates: Gypsum, bassanite, and anhydrite. *Am. Mineral.* **2014**, *99*, 2105–2115. [CrossRef]
54. Bhattacharya, S.; Mitra, S.; Gupta, S.; Jain, N.; Chauhan, P.; Parthasarathy, G. Jarosite occurrence in the Deccan Volcanic Province of Kachchh, western India: Spectroscopic studies on a Martian analog locality. *J. Geophys. Res.* **2016**, *121*, 402–431. [CrossRef]
55. Calvo, M.; Sevillano, E. Pyrite crystals from Soria and La Rioja provinces, Spain. *Mineral. Mag.* **1989**, *20*, 451–456.
56. Kölbl, D.; Pignitter, M.; Somoza, V.; Schimak, M.P.; Strbak, O.; Blazevic, A.; Milojevic, T. Exploring fingerprints of the extreme thermoacidophile Metallosphaera sedula grown on synthetic martian regolith materials as the sole energy sources. *Front. Microbiol.* **2017**, *8*, 1918. [CrossRef]
57. Zalewska, N.E.; Mroczkowska-Szerszeń, M.; Fritz, J.; Błęcka, M. Modeling of surface spectra with and without dust from Martian infrared data: New aspects. *Aircr. Eng. Aerosp. Technol.* **2019**, *91*, 333–345. [CrossRef]
58. Zolotov, M.Y.; Shock, E.L. Formation of jarosite-bearing deposits through aqueous oxidation of pyrite at Meridiani Planum, Mars. *Geophys. Res. Lett.* **2005**, *32*, 90. [CrossRef]
59. Schwenzer, S.P.; Abramov, O.; Allen, C.C.; Bridges, J.C.; Clifford, S.M.; Filiberto, J.; Kring, D.A.; Lasue, J.; McGovern, P.J.; Newsom, H.E.; et al. Gale Crater: Formation and post-impact hydrous environments. *Planet. Space Sci.* **2012**, *70*, 84–95. [CrossRef]
60. Yen, A.S.; Morris, R.V.; Clark, B.C.; Gellert, R.; Knudson, A.T.; Squyres, S.; Mittlefehldt, D.W.; Ming, D.W.; Arvidson, R.; McCoy, T.; et al. Hydrothermal processes at Gusev Crater: An evaluation of Paso Robles class soils. *J. Geophys. Res. E Planets* **2008**, *113*, 108. [CrossRef]
61. De Angelis, S.; Manzari, P.; De Sanctis, M.C.; Altieri, F.; Carli, C.; Agrosì, G. Application of spectral linear mixing to rock slabs analyses at various scales using Ma_Miss BreadBoard instrument. *Planet. Space Sci.* **2017**, *144*, 1–15. [CrossRef]
62. Shi, C.; Wang, L. Incorporating spatial information in spectral unmixing: A review. *Remote Sens. Environ.* **2014**, *149*, 70–87. [CrossRef]
63. Ramsey, M.S.; Christensen, P.R. Mineral abundance determination: Quantitative deconvolution of thermal emission spectra. *J. Geophys. Res. Solid Earth* **1998**, *103*, 577–596. [CrossRef]
64. Lyon, R. Analysis of rocks by spectral infrared emission (8 to 25 microns). *Econ. Geol.* **1965**, *60*, 715–736. [CrossRef]
65. Thomson, J.L.; Salisbury, J.W. The Mid-Infrared Reflectance of Mineral Mixtures (7–14/m). *Remote Sens. Environ.* **1993**, *13*, 1–13. [CrossRef]
66. Smith, M.D.; Bandfield, J.L.; Christensen, P.R. Separation of atmospheric and surface spectral features in Mars Global Surveyor Thermal Emission Spectrometer (TES) spectra. *J. Geophys. Res.* **2000**, *105*, 9589. [CrossRef]
67. Christensen, P.R.; Bandfield, J.L.; Smith, M.D.; Hamilton, V.E.; Clark, R.N. Identification of a basaltic component on the Martian surface from Thermal Emission Spectrometer data spectra of Mars during the initial aerobraking and science-phasing. *J. Geophys. Res. Plants* **2000**, *105*, 9609–9621. [CrossRef]
68. Bishop, J.L.; Michalski, J.R.; Carter, J. *Remote Detection of Clay Minerals*, 1st ed.; Elsevier Ltd.: Amsterdam, The Netherlands, 2017; Volume 8, ISBN 9780081003558.
69. Zalewska, N. Modeling of Sprectra With and Without Dust from Martian Surface Based on Infrared Data. *Trans. Inst. Aviat.* **2016**, *245*, 287–308. [CrossRef]
70. Martin-Izard, A.; Arias, D.; Arias, M.; Gumiel, P.; Sanderson, D.J.; Castañon, C.; Lavandeira, A.; Sanchez, J. A new 3D geological model and interpretation of structural evolution of the world-class Rio Tinto VMS deposit, Iberian Pyrite Belt (Spain). *Ore Geol. Rev.* **2015**, *71*, 457–476. [CrossRef]
71. Connerney, J.E.P.; Acuña, M.H.; Ness, N.F.; Kletetschka, G.; Mitchell, D.L.; Lin, R.P.; Reme, H. Tectonic implications of Mars crustal magnetism. *Proc. Natl. Acad. Sci. USA* **2005**, *102*, 14970–14975. [CrossRef] [PubMed]
72. Lenardic, A.; Nimmo, F.; Moresi, L. Growth of the hemispheric dichotomy and the cessation of plate tectonics on Mars. *J. Geophys. Res. E Planets* **2004**, *109*, 53. [CrossRef]
73. Bouley, S.; Baratoux, D.; Paulien, N.; Missenard, Y.; Saint-Bézar, B. The revised tectonic history of Tharsis. *Earth Planet. Sci. Lett.* **2018**, *488*, 126–133. [CrossRef]
74. Mège, D.; Masson, P. A plume tectonics model for the Tharsis province, Mars. *Planet. Space Sci.* **1996**, *44*, 1499–1546. [CrossRef]
75. Skok, J.R.; Mustard, J.F.; Ehlmann, B.L.; Milliken, R.E.; Murchie, S.L. Silica deposits in the Nili Patera caldera on the Syrtis Major volcanic complex on Mars. *Nat. Geosci.* **2010**, *3*, 838–841. [CrossRef]
76. Schulze-Makuch, D.; Dohm, J.M.; Fan, C.; Fairén, A.G.; Rodriguez, J.A.P.; Baker, V.R.; Fink, W. Exploration of hydrothermal targets on Mars. *Icarus* **2007**, *189*, 308–324. [CrossRef]
77. Michalski, J.R.; Dobrea, E.Z.N.; Niles, P.B.; Cuadros, J. Ancient hydrothermal seafloor deposits in Eridania basin on Mars. *Nat. Commun.* **2017**, *8*, 15978. [CrossRef]
78. Osinski, G.R.; Tornabene, L.L.; Banerjee, N.R.; Cockell, C.S.; Flemming, R.; Izawa, M.R.M.; Mccutcheon, J.; Parnell, J.; Preston, L.J.; Pickersgill, A.E.; et al. Impact-generated hydrothermal systems on Earth and Mars. *Icarus* **2013**, *224*, 347–363. [CrossRef]

79. Dare, S.A.S.; Barnes, S.J.; Prichard, H.M. The distribution of platinum group elements (PGE) and other chalcophile elements among sulfides from the Creighton Ni-Cu-PGE sulfide deposit, Sudbury, Canada, and the origin of palladium in pentlandite. *Miner. Depos.* **2010**, *45*, 765–793. [CrossRef]
80. Frimmel, H.E. Detrital origin of hydrothermal Witwatersrand goldÐa review. *Terra Nova* **1997**, *9*, 192–197. [CrossRef]
81. Li, C.; Naldrett, A.J. A numerical model for the compositional variations of Sudbury sulfide ores and its application to exploration. *Economic* **1994**, *89*, 1599–1607. [CrossRef]
82. Dare, S.A.S.; Barnes, S.J.; Prichard, H.M.; Fisher, P.C. Chalcophile and platinum-group element (PGE) concentrations in the sulfide minerals from the McCreedy East deposit, Sudbury, Canada, and the origin of PGE in pyrite. *Miner. Depos.* **2011**, *46*, 381–407. [CrossRef]
83. Brož, P.; Hauber, E.; Wray, J.J.; Michael, G. Amazonian volcanism inside Valles Marineris on Mars. *Earth Planet. Sci. Lett.* **2017**, *473*, 122–130. [CrossRef]
84. Hawkins, G.J.; Sherwood, R.E.; Djotni, K.; Threadgold, T.M. Cooled optical filters for Q -band infrared astronomy (15–40 μm). *Adv. Opt. Mech. Technol. Telesc. Instrum. II* **2016**, *9912*, 991235. [CrossRef]
85. Lennie, A.R.; Vaughan, D.J. Kinetics of the marcasite-pyrite transformation: An infrared spectroscopic study. *Am. Mineral.* **1992**, *77*, 1166–1171.
86. Rigopoulou, D.; Pearson, C.; Ellison, B.; Wiedner, M.; Okada, V.O.; Tan, B.K.; Garcia-Bernete, I.; Gerin, M.; Yassin, G.; Caux, E.; et al. The far-infrared spectroscopic surveyor (FIRSS). *Exp. Astron.* **2021**, *51*, 699–728. [CrossRef]
87. Kendix, E.; Moscardi, G.; Mazzeo, R.; Baraldi, P.; Prati, S.; Joseph, E.; Capelli, S. Far infrared and Raman spectroscopy analysis of inorganic pigments. *J. Raman Spectrosc.* **2008**, *39*, 1104–1112. [CrossRef]
88. Murad, E.; Bishop, J.L. The infrared spectrum of synthetic akaganeite, β-FeOOH. *Am. Mineral.* **2000**, *85*, 716–721. [CrossRef]
89. Salisbury, J.W.; Walter, L.S.; Vergo, N. Availability of a library of infrared (2.1–25.0 μm) mineral spectra. *Am. Mineral.* **1989**, *74*, 938–939.
90. Stimson, M.; O'Donnell, M. The Infrared and Ultraviolet Absorption Spectra of Cytosine and Isocytosine in the Solid State. *J. Am. Chem. Soc.* **1952**, *74*, 1805–1808. [CrossRef]
91. Salisbury, J.W.; Walter, L.S.; Vergo, N. Mid-infrared (2.1–25 um) spectra of minerals: First edition. *USGS Open-File Rep.* **1987**, 390.